Electric Field and Strain Tuning of 2D Semiconductor van der Waals Heterostructures for Tunnel Field-Effect Transistors

Citation for the original published paper (version of record):
Iordanidou, K., Mitra, R., Shetty, N. et al (2022). Electric Field and Strain Tuning of 2D
Semiconductor van der Waals Heterostructures for Tunnel
Field-Effect Transistors. ACS Applied Materials & Interfaces, In Press.
http://dx.doi.org/10.1021/acsami.2c13151

(article starts on next page)

ACS APPLIED MATERIALS & INTERFACES

www.acsami.org

Research Article

Electric Field and Strain Tuning of 2D Semiconductor van der Waals Heterostructures for Tunnel Field-Effect Transistors

Konstantina Iordanidou,* Richa Mitra, Naveen Shetty, Samuel Lara-Avila, Saroj Dash, Sergey Kubatkin, and Julia Wiktor

Cite This: https://doi.org/10.1021/acsami.2c13151

Read Online

ACCESS | Metrics & More | Article Recommendations | Supporting Information

ABSTRACT: Heterostacks consisting of low-dimensional materials are attractive candidates for future electronic nanodevices in the post-silicon era. In this paper, using first-principles calculations based on density functional theory (DFT), we explore the structural and electronic properties of $MoTe_2/ZrS_2$ heterostructures with various stacking patterns and thicknesses. Our simulations show that the valence band (VB) edge of $MoTe_2$ is almost aligned with the conduction band (CB) edge of ZrS_2, and $(MoTe_2)_m/(ZrS_2)_m$ (m = 1, 2) heterostructures exhibit the long-sought broken gap band alignment, which is pivotal for realizing tunneling transistors. Electrons are found to spontaneously flow from $MoTe_2$ to ZrS_2, and the system resembles an ultrascaled parallel plate capacitor with an intrinsic electric field pointed from $MoTe_2$ to ZrS_2. The effects of strain and external electric fields on the electronic properties are also investigated. For vertical compressive strains, the charge transfer increases due to the decreased coupling between the layers, whereas tensile strains lead to the opposite behavior. For negative electric fields a transition from the type-III to the type-II band alignment is induced. In contrast, by increasing the positive electric fields, a larger overlap between the valence and conduction bands is observed, leading to a larger band-to-band tunneling (BTBT) current. Low-strained heterostructures with various rotation angles between the constituent layers are also considered. We find only small variations in the energies of the VB and CB edges with respect to the Fermi level, for different rotation angles up to 30°. Overall, our simulations offer insights into the fundamental properties of low-dimensional heterostructures and pave the way for their future application in energy-efficient electronic nanodevices.

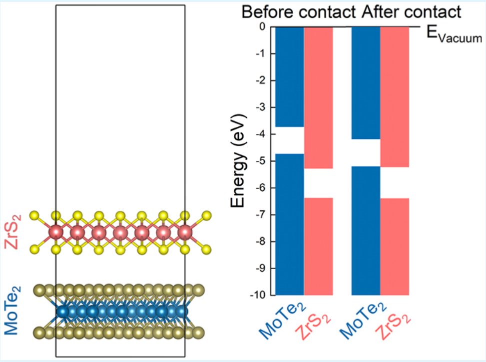

KEYWORDS: *2D heterostructures, band alignment, electronic properties, external electric field, strain*

1. INTRODUCTION

The downscaling of the transistors has resulted in improved power efficiencies. However, an additional decrease of the transistor size can cause a significant rise in power consumption and heat production. One of the major issues is the so-called Boltzmann's limit which restricts the subthreshold swing at 60 mV/dec at room temperature and prevents the reduction of the supply voltage as the size of the transistor is reduced. As a solution to this issue, other transistor architectures, e.g., the tunneling transistors, have been proposed.[1−3]

For traditional transistors, electrons are thermally injected over a potential barrier, whereas for tunnel field-effect transistors (TFETs) the conduction mechanism is the band-to-band tunneling current. Two-dimensional heterostructures with van der Waals interactions between the layers are attractive candidates for future TFETs. Their ideal (free of dangling bonds) interfaces can prevent the trap-assisted tunneling current, and their band alignments can be effectively manipulated by applying gate voltages. In addition, due to the weak interaction between the layers, the constraint of lattice matching is not valid, and appealing van der Waals heterostructures (vdWH) composed of various materials can be realized.[4−10]

Transition-metal dichalcogenide (TMD) monolayers are among the most promising 2D materials for next-generation nanoelectronic applications,[11,12] and their vertical/lateral stacks have been intensively investigated.[13,14] 2D ZrS_2 has been successfully synthesized via an electrochemical lithiation process whereas 2D $MoTe_2$ has been fabricated through, e.g., the liquid exfoliating technique.[15,16] At room temperature, the calculated phonon-limited mobilities are as high as ~2500 and 1200 $cm^2\ V^{-1}\ s^{-1}$ for 2D $MoTe_2$ and ZrS_2, respectively.[17]

Through density functional theory (DFT) simulations, the structural and electronic properties of $MoTe_2/ZrS_2$ hetero-

Received: July 22, 2022
Accepted: November 21, 2022

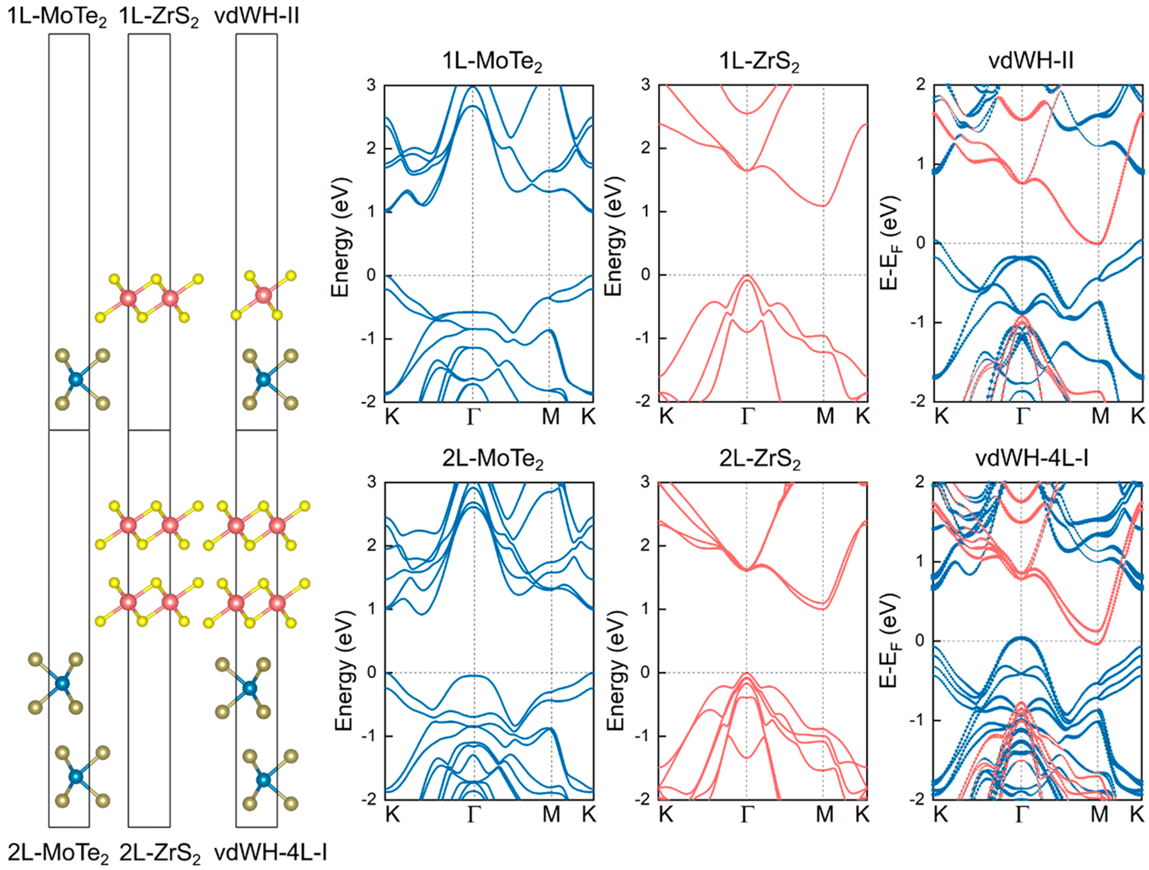

Figure 1. Relaxed atomic structures and electronic band structures of monolayer $MoTe_2$ (1L-$MoTe_2$), monolayer ZrS_2 (1L-ZrS_2), and their favorable heterostack (vdWH-II) (upper panels). Relaxed atomic structures and electronic band structures of bilayer $MoTe_2$ (2L-$MoTe_2$), bilayer ZrS_2 (2L-ZrS_2) and their favorable heterostack (vdWH-4L-I) (lower panels). Blue, brown, orange and yellow spheres correspond to Mo, Te, Zr, and S atoms, respectively. For the band structures of the single-layer and bilayer systems the energies refer to the VB edge. SOC is included in the calculations.

structures with various stacking patterns are explored. Our simulations show that the valence band (VB) edge of $MoTe_2$ is almost aligned with the conduction band (CB) edge of ZrS_2, and the heterostructures exhibit the type-III or broken gap band alignment, which is pivotal for realizing tunneling transistors. The effects of external electric fields and strain on the electronic properties are also investigated.

It is worth noting that contrary to many theoretical studies focusing on hypothetical 2D materials, our work is devoted to 2D materials which are stable and can be experimentally synthesized. Furthermore, many theoretical investigations consider only one model for the van der Waals heterostructure and limit their analysis to single layers whereas experimentalists may have difficulties to reach the monolayer regime. For instance, $MoTe_2$/$SnSe_2$ heterostructures have been proved to be promising for future tunneling transistors, but the investigation was focused only on monolayer materials.[18] Our study overcomes these limitations, and our work can inspire experimentalists to realize tunneling transistors with optimal performance.

2. MODELS AND COMPUTATIONAL METHODS

Our calculations were performed using DFT as implemented in the Vienna Ab initio Simulation Package (VASP).[19,20] We employed the projected augmented wave (PAW) pseudopotentials[21] with valence electron configurations of $4s^2 4p^6 4d^5 5s^1$ for Mo, $5s^2 5p^4$ for Te, $4s^2 4p^6 4d^2 5s^2$ for Zr, and $3s^2 3p^4$ for S. Low-strained heterobilayers were constructed using the Cellmatch code,[22] and periodic slabs with ~20 Å vacuum were considered. Through the rev-vdW-DF2 functional, dispersion corrections were utilized in the optimizations and total energy computations.[23] The rest of the calculations were performed using the Perdew, Burke, and Ernzerhof (PBE) functional.[24]

The structures were optimized using the conjugate gradient method with 0.01 eV/Å force convergence criteria and 10^{-8} eV energy convergence criteria. The kinetic energy cutoff was set to 500 eV, and the Brillouin zone was sampled by a $4 \times 4 \times 1$ k-mesh for the low-strained heterobilayers consisting of 75 atoms, whereas a $16 \times 16 \times 1$ k-mesh was considered for the (1×1) $MoTe_2$/(1×1) ZrS_2 heterostructures. Energy convergence tests with respect to the number of k-points have been performed, and we concluded that a $4 \times 4 \times 1$ k-grid results in well-converged results. Furthermore, the effects of relativistic interactions on the electronic properties were investigated. We computed the band structures with SOC by employing the PBE generalized gradient approximation and by using the rev-vdW-DF2 relaxed heterostructures, following the methodology in similar studies.[18,25] To overcome the underestimation of the band gap of standard DFT, hybrid functional calculations were additionally performed using the HSE06 functional.[26] For calculations under E_{ext} and for the calculation of the average electrostatic potential, dipole corrections were also included perpendicular to the *ab*-plane.

3. RESULTS AND DISCUSSION

3.1. Structural and Electronic Properties of $(MoTe_2)_m$/$(ZrS_2)_m$ (m = 1, 2) vdWH.

As shown in Figure 1, monolayers $MoTe_2$ and ZrS_2 consist of two hexagonal chalcogen planes separated by one hexagonal metal plane. $MoTe_2$ adopts the trigonal-prismatic geometry whereas ZrS_2 the octahedral one. The in-plane lattice constants are 3.530 and 3.659 Å for $MoTe_2$ and ZrS_2 respectively, and their lattice mismatch is ~4%. As a first step, we construct heterobilayers by simply stacking $MoTe_2$ and ZrS_2 unit cells and by equally distributing the strain within the layers; i.e., $MoTe_2$ is stretched by ~2% whereas ZrS_2 is compressed by the same amount. Optimizations are performed to relax the atomic positions whereas the lattice constants are kept fixed. For our study, we consider configurations with different stacking patterns of high symmetry, namely vdWH-I, vdWH-II, vdWH-III, vdWH-IV, vdWH-V, and vdWH-VI (see the Supporting Information, Figure S1). Our calculations reveal that the most stable structure corresponds to vdWH-II for which Zr atoms are located above Mo atoms whereas top-layer S atoms lie above Te atoms. Notably, the total energy of vdWH-IV is only 0.07 meV/atom larger as compared to the lowest energy structure. For vdWH-IV, the bottom-layer S atoms are above Mo atoms whereas the top-layer S atoms are above Te atoms. To verify that our findings do not depend on the selection of the van der Waals functional, OptB86b-vdW and vdW-DF-cx calculations as well as PBE calculations including the Grimme-D3 corrections[27−29] are also performed, leading to similar results (see the Supporting Information, Table S1).

For the lowest energy structure, the interlayer distance between $MoTe_2$ and ZrS_2 layers is d_{int} = 3.1 Å, whereas for all other considered configurations the interlayer distances range from 3.1 to 3.7 Å. These results are also verified by using various van der Waals functionals (see the Supporting Information, Table S1). The calculated interlayer distances are in good agreement with the findings of previous investigations. For instance, Lu et al. performed a systematic study of 120 heterobilayers composed of various TMDs, graphene, and hexagonal boron nitride, and the interlayer distances were found to range from about 3 to 4 Å. In their study, a heterobilayer consisting of 1H-$MoTe_2$ and 1H-ZrS_2 with d_{int} = 3.19 Å was also reported.[30] In our test calculations, considering the same heterobilayer and the same stacking pattern d_{int} = 3.10 Å, which is in good agreement with the corresponding value reported in the literature. Notably, the interlayer distances should be predicted as accurately as possible to ensure a proper description of the orbital hybridization, electron charge transfer, electronic structure, etc. A recent paper reports 1H-$MoTe_2$/1T-ZrS_2 heterobilayers having our the so-called vdWH-IV stacking pattern and an interlayer distance of 2.75 Å,[31] which is slightly lower compared to our computed values using various van der Waals functionals.

Next, the binding energy is calculated through the equation

$$E_b = E_t(MoTe_2/ZrS_2) - E_t(MoTe_2) - E_t(ZrS_2) \qquad (1)$$

where $E_t(MoTe_2/ZrS_2)$ refers to the total energy of the heterobilayer whereas $E_t(MoTe_2)$ and $E_t(ZrS_2)$ refer to the total energies of the isolated (strained) monolayers. For the lowest energy heterobilayer we find $E_b = -23$ meV/Å^2, and the negative sign reveals its structural stability. The binding energies of the other considered configurations are also negative, ranging from −23 to −14 meV/Å^2.

With regard to the electronic properties, using the PBE functional and including SOC, monolayer $MoTe_2$ exhibits a direct band gap of 1.00 eV whereas ZrS_2 has an indirect band gap of 1.09 eV, in agreement with previously reported simulations.[32] Figure 1 shows the band structure of the lowest energy heterobilayer, and similar results are observed in all other heterobilayers (see the Supporting Information, Figures S2 and S3). The energy difference between the ZrS_2 conduction band edge and $MoTe_2$ valence band edge is $E_{CBM-VBM} = -0.05$ eV. Neglecting spin−orbit coupling the band gaps are found to be slightly larger by 0.13 and 0.04 eV for $MoTe_2$ and ZrS_2, respectively, and for the heterobilayer $E_{CBM-VBM}$ is found to be −0.02 eV. DFT typically underestimates the energy gaps, and to overcome this limitation HSE06 calculations are also performed. Using HSE06 and including SOC, the energy difference between the CB and VB edges is −0.02 eV. Overall, our calculations reveal that $MoTe_2$/ZrS_2 heterobilayer exhibits the type-III or broken gap band alignment, with a slight overlap between the VB and CB states, which is highly promising for realizing tunneling transistors.

In line with our findings, Reddy et al. explored heterostructures composed of WSe_2 and $SnSe_2$, and they proved the occurrence of semimetallicity through various transport measurements.[33] For instance, semimetallicity was revealed by the coexistence of holes and electrons, observed by the Hall slope evolution with lowering the temperature or with sweeping the gate voltage. In their study it was pointed out that the transport properties of WSe_2/$SnSe_2$ interfaces were significantly different compared to the transport properties of the constituent layers which exhibit sizable band gaps. Although our work was focused on heterostructures composed of $MoTe_2$ and ZrS_2, the band alignments of various 2D materials with respect to the vacuum level were also computed (see the Supporting Information, Figure S4), and other combinations of 2D materials that are potentially promising for realizing the type-III band alignment could be identified.

Because of the charge transfer/redistribution and the interfacial dipole formation, the band structure of the heterobilayer is not an exact combination of the band structures of the constituent layers. To accurately assess the effect of stacking on the electronic structure, we compute the band structures of the isolated $MoTe_2$ and ZrS_2 monolayers, having the same lattice parameters as those in the heterobilayer. Considering the heterobilayer, the band gaps of $MoTe_2$ and ZrS_2 are found to be 0.85 and 0.91 eV, respectively, whereas for the noninteracting monolayers the band gaps are 0.86 and 0.87 eV. Furthermore, for the heterobilayer, the $MoTe_2$ topmost valence band exhibits a Rashba-like splitting around the Γ-point, which is not observed in the band structure of the isolated system. Although isolated monolayer $MoTe_2$ exhibits an out-of-plane mirror symmetry, by placing ZrS_2 on top of $MoTe_2$, the symmetry breaks and the Rashba effect occurs. Considering the KΓ direction, the energy difference and the (maximum) momentum offset between the band extremum around the Γ-point and the band degenerate Γ-point are $E_R = 0.015$ eV and $k_R = 0.12$ Å^{-1}, respectively.

To comment on the transport properties, we calculated the electron effective masses by fitting a parabola to the conduction band minimum.[34] In particular, the effective masses are derived from the band structures using the formula $1/m^* = \partial^2 E(k)/(\hbar^2 \partial k^2)$, where $E(k)$ is the k-resolved energy of the band and $\hbar$ is the reduced Planck constant. For the parabolic fitting a region of 0.08 Å^{-1} is considered.

First, the electron effective masses of the isolated (strain-free) monolayers are computed. For $MoTe_2$, the effective masses along the MK and ΓK directions are $m_{e,MK} = 0.62m_0$ and $m_{e,\Gamma K} = 0.54m_0$. Accordingly, for ZrS_2 the effective masses in the ΓM and KM directions are $m_{e,\Gamma M} = 1.99m_0$ and $m_{e,KM}$ =

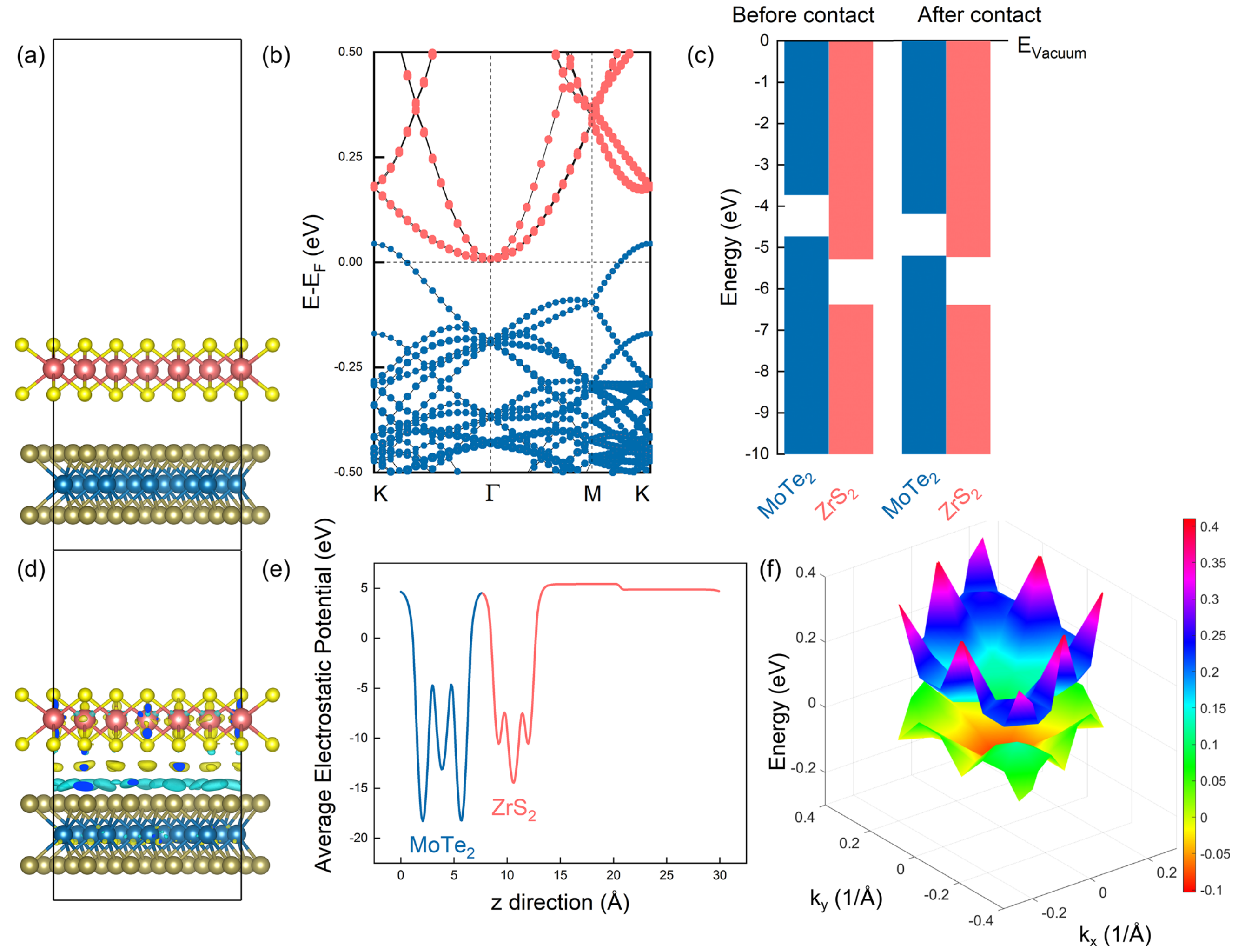

Figure 2. Relaxed atomic structure of low-strained $MoTe_2/ZrS_2$ heterobilayer with rotated layers and its corresponding band structure (a, b). Band alignment with respect to the vacuum level prior and after the heterobilayer formation (c). Charge density difference $\Delta\rho_c = \rho_c(MoTe_2/ZrS_2) - \rho_c(MoTe_2) - \rho_c(ZrS_2)$ and average electrostatic potential along the *z*-axis (d, e). 3D band structure, obtained using VASPKIT,[44] of the topmost VB and the bottommost CB (f). Blue (orange) lines refer to contributions from $MoTe_2$ (ZrS_2) monolayers. Yellow (blue) isosurfaces correspond to electron accumulation (depletion). The isosurface value is set to 0.0005 electrons/bohr^3. SOC is included in the calculations.

$0.30m_0$, and these results are in good agreement with previously reported theoretical calculations.[17] For the heterobilayer, the CB is originated from ZrS_2, and considering the energetically favorable configuration, we find $m_{e,\Gamma M} = 1.92m_0$ and $m_{e,KM} = 0.26m_0$. Overall, heavy effective masses indicate low mobilities, whereas light effective masses correspond to high mobilities.

Heterostructures with various rotation angles between the constituting layers can be experimentally realized.[35−37] Therefore, we next perform rotations of ZrS_2 with respect to $MoTe_2$, and we look for stacks with the number of atoms <100 and strain <1%. The selected stack consists of $(\sqrt{13} \times \sqrt{13})MoTe_2$ and $(\sqrt{12} \times \sqrt{12})ZrS_2$ layers with a relative rotation between the layers of ~16°. In this model, $MoTe_2$ lattice constants remain unchanged whereas ZrS_2 accommodates the total strain of ~0.4%. Such small strain has a minor impact on the electronic structure of single-layer ZrS_2, and a minor impact on the electronic structure of the heterobilayer is expected. For the selected stack various translation operations have been performed. We move monolayer ZrS_2 in the *a*/*b* directions, and we consider shifts of 0.2*a* or/and 0.2*b*. Optimizations are performed for every shift, and for the most stable and least stable structures the energy difference is 0.01 meV/atom. The binding energy of the heterobilayer with rotated layers is found to be −18 meV/Å^2, and the negative sign reveals its structural stability.

Figure 2 presents the band structure of the low-strained $MoTe_2/ZrS_2$ vdWH with rotated layers and the band alignment prior and after forming the heterostructure. It is worth mentioning that the band alignment prior to forming the heterostructure corresponds to the unit cells without strain. Using the PBE functional with SOC, the energy difference between the CB and VB edges is found to be −0.04 eV, and the heterobilayer exhibits the type-III band alignment similar to the (1 × 1) $MoTe_2$/(1 × 1) ZrS_2 stack. Because the work function of $MoTe_2$ is lower than that of ZrS_2,[32] electrons spontaneously flow from $MoTe_2$ to ZrS_2 when the heterostructure is formed. The Bader charge analysis reveals that ~3 × 10^{13} e/cm^2 are transferred from the one layer to the other. As a next step, the charge density difference is computed through the formula $\Delta\rho_c = \rho_c(MoTe_2/ZrS_2) - \rho_c(MoTe_2) - \rho_c(ZrS_2)$, where $\rho_c(MoTe_2/ZrS_2)$ refers to the charge density of the heterobilayer whereas $\rho_c(MoTe_2)$ and $\rho_c(ZrS_2)$ refer to the charge densities of the monolayers. We find that Te atoms of the upper layer and S atoms of the lower layer mainly participate in the electron transfer process. In agreement with the Bader charge analysis, $MoTe_2$ and ZrS_2 exhibit electron depletion and accumulation, respectively, and the heterobilayer resembles an ultrascaled parallel plate capacitor with an intrinsic electric field pointed from $MoTe_2$ to ZrS_2.

Next, heterobilayers with other rotation angles between the constituting layers are briefly discussed. We construct low-strained heterostructures with relative rotations of 10° and 30°, having 177 and 156 total number of atoms, respectively. Using the PBE functional and including SOC, the energy difference between the CB and VB edges is found to be negative, similar to the previously discussed heterobilayers (see the Supporting Information, Figure S5). Overall, our simulations reveal that heterostructures composed of 2D $MoTe_2$ and ZrS_2 with different stacking patterns present band alignments which are highly promising for tunneling transistors.

As a next step, we explore thicker heterostructures composed of $MoTe_2$ and ZrS_2 bilayers. As shown in Figure 1, for $MoTe_2$ we consider the 2H-stacking where Mo atoms of the top layer are located above Te atoms of the bottom layer, and vice versa. For ZrS_2 the two layers are placed on top of each other without any shift or rotation, and these stackings correspond to the lowest energy structures.[38−40] With regard to the structural properties, the in-plane lattice constants of $MoTe_2$ and ZrS_2 bilayers are 3.533 and 3.655 Å, respectively, and their lattice mismatch is ∼3%. Because of the relatively low lattice mismatch, we can construct heterostructures by simply stacking the corresponding unit cells and by equally distributing the total strain within the layers. Similar to the previous analysis, we consider six high symmetry systems, namely vdWH-4L-I, vdWH-4L-II, vdWH-4L-III, vdWH-4L-IV, vdWH-4L-V, and vdWH-4L-VI (see the Supporting Information, Figure S6). We find that the energetically favorable structure corresponds to vdWH-4L-I, for which the bottom layer S atoms are located above Mo atoms whereas the top-layer S atoms lie above Te atoms. Notably, the total energy of vdWH-4L-V is only 0.14 meV/atom larger as compared to the energy of vdWH-4L-I (see the Supporting Information, Table S2). For the most stable structure the interlayer distance is 3.1 Å, whereas for all other systems it ranges from 3.1 to 3.7 Å (see the Supporting Information, Table S2). Also, for the most stable structure the binding energy is -24 meV/$Å^2$, which is nearly equal to the binding energy of the favorable heterobilayer.

Our PBE calculations including SOC show that bilayer $MoTe_2$ has an indirect gap of 0.92 eV whereas bilayer ZrS_2 presents an indirect gap of 1.00 eV. For the bilayers the energy gaps are slightly lower as compared to the monolayer systems. Omitting SOC, the band gaps are larger by 0.06 and 0.04 eV for $MoTe_2$ and ZrS_2, respectively. Figure 1 shows the band structure of the energetically favorable heterostructure whereas heterostructures with other stacking patterns present similar band structures (see the Supporting Information, Figures S7 and S8). Interestingly, the heterostructure formed by bilayer $MoTe_2$ and bilayer ZrS_2 exhibits the type-III or broken gap band alignment. This means that in practical realizations of tunneling transistors it may not be crucial to achieve thicknesses in the monolayer regime. Using the PBE functional and taking into account SOC, the energy difference between the ZrS_2 CB edge and $MoTe_2$ VB edge is -0.08 eV, i.e., slightly lower compared to the corresponding values in the studied heterobilayers.

To evaluate the exact effect of stacking on the electronic structure, we compute the band structures of the isolated $MoTe_2$ and ZrS_2 bilayers, having the same lattice parameters as those in the heterostructure. Considering the heterostructure, the band gaps of bilayer $MoTe_2$ and ZrS_2 are found to be 0.62 and 0.74 eV, respectively, whereas for the noninteracting bilayers the gaps are 0.73 and 0.78 eV. It is worth noting that for the strained isolated $MoTe_2$ bilayer the VB edge shifts from the K- to the Γ-point, as compared to the strain-free system, and this shift is also observed in the band structure of the heterostructure. Notably, for the heterostructure the two highest energy valence bands (originated from $MoTe_2$) present a significant splitting around the K-point which is not observed in the band structure of the isolated $MoTe_2$ bilayer or the isolated slightly stained $MoTe_2$ bilayer. The splitting of the bands can be attributed to the break of the symmetry upon stacking. For our investigation, we consider the 2H-stacked bilayer having the inversion symmetry which later breaks by the presence of ZrS_2. Considering the so-called R-stacked bilayer $MoTe_2$ which lacks the inversion symmetry, the splitting of the topmost valence bands around the K-point is observed in its band structure (see the Supporting Information, Figure S9).

For the sake of completeness, we explore heterostructures composed of $MoTe_2$ monolayers and ZrS_2 bilayers (or $MoTe_2$ bilayers and ZrS_2 monolayers). For the constructed stacks the strain is equally distributed between $MoTe_2$ and ZrS_2, and various stacking patterns of high symmetry are considered, namely vdWH-3L-I, vdWH-3L-II, vdWH-3L-III, vdWH-3L-IV, vdWH-3L-V, and vdWH-3L-VI (or vdWH-3L′-I, vdWH-3L′-II, vdWH-3L′-III, vdWH-3L′-IV, vdWH-3L′-V, and vdWH-3L′-VI) (see the Supporting Information, Figures S10 and S11). The two energetically favorable configurations correspond to vdWH-3L-II and vdWH-3L-IV (or vdWH-3L′-I and vdWH-3L′-V). These configurations are structurally equivalent to the lowest energy configurations observed by stacking monolayer materials (vdWH-II and vdWH-IV) or bilayer materials (vdWH-4L-I and vdWH-4L-V). The binding energies of the heterostructures are found to be negative, i.e., -23 meV/Å for vdWH-3L-II and -24 meV/Å for vdWH-3L′-I. Our PBE calculations including SOC reveal that the heterostructures present the type-III band alignment (see the Supporting Information, Figures S12 and S13). The energy difference between the CB and VB edges is -0.06 and -0.07 eV for vdWH-3L-II and vdWH-3L′-I, respectively. For calculations without SOC, we find similar results (see the Supporting Information, Figures S14 and S15).

As a last step, we examine heterostructures composed of $MoTe_2$ monolayers and ZrS_2 trilayers/tetralayers (or ZrS_2 monolayers and $MoTe_2$ trilayers/tetralayers). In line with the previous analysis, the strain is equally distributed between $MoTe_2$ and ZrS_2, whereas only two possible configurations of high symmetry are considered (see the Supporting Information, Figures S16 and S17). These configurations are structurally equivalent to the lowest energy configurations, observed by stacking monolayer materials or bilayer materials or monolayer along with bilayer materials. With regard to the electronic properties, our PBE calculations including SOC show that trilayer and tetralayer $MoTe_2$ are semiconductors with indirect band gaps of 0.82 and 0.79 eV, respectively. Accordingly, trilayer and tetralayer ZrS_2 exhibit indirect band gaps of 0.96 and 0.95 eV, respectively. Notably, the heterostructures present the broken gap band alignment, and

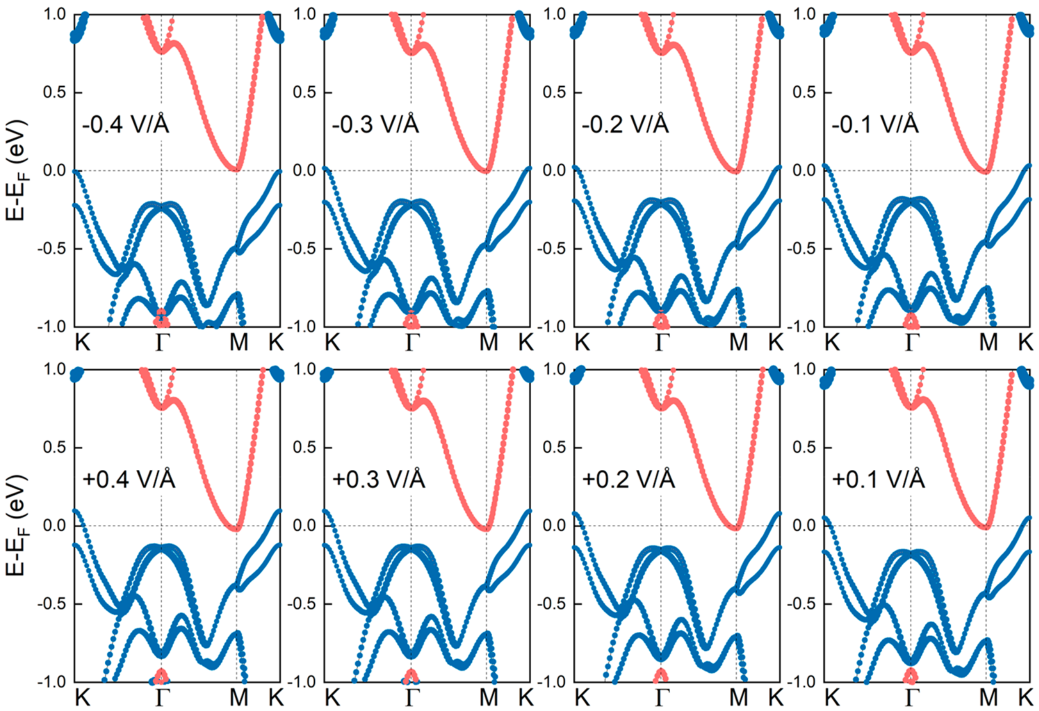

Figure 3. Electronic band structures of (1 × 1) $MoTe_2$/(1 × 1) ZrS_2 heterobilayers in the presence of E_{ext}. Blue (orange) lines refer to contributions from $MoTe_2$ (ZrS_2) monolayers. SOC is included in the calculations.

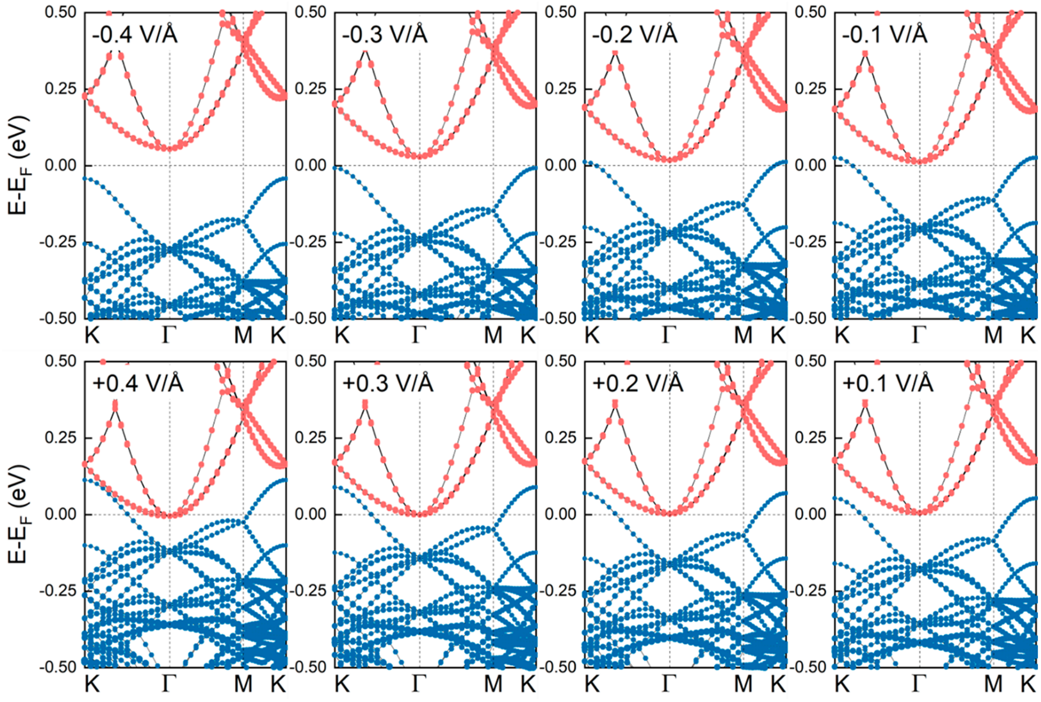

Figure 4. Electronic band structures of low-strained $MoTe_2$/ZrS_2 heterobilayers with rotated layers in the presence of E_{ext}. Blue (orange) lines refer to contributions from $MoTe_2$ (ZrS_2) monolayers. SOC is included in the calculations.

for calculations without SOC we find similar results (see the Supporting Information, Figures S18 and S19).

3.2. Application of Electric Field. Next, we examine the electronic properties of $MoTe_2$/ZrS_2 heterobilayers in the presence of external electric fields (E_{ext}). The electric field is imposed in the vertical direction, and its strength varies from −0.4 to 0.4 V/Å. Positive values correspond to electric fields pointed from $MoTe_2$ to ZrS_2, whereas negative values correspond to the opposite orientation. In our study, both optimizations and band structure calculations are performed under the electric field application.

The electric field induces a potential gradient normal to the interface and results in the redistribution of the charge carriers along the layers. The charge redistribution can significantly impact the band edge positions, and Figure 3 shows the electronic band structures of (1 × 1) $MoTe_2$/(1 × 1) ZrS_2

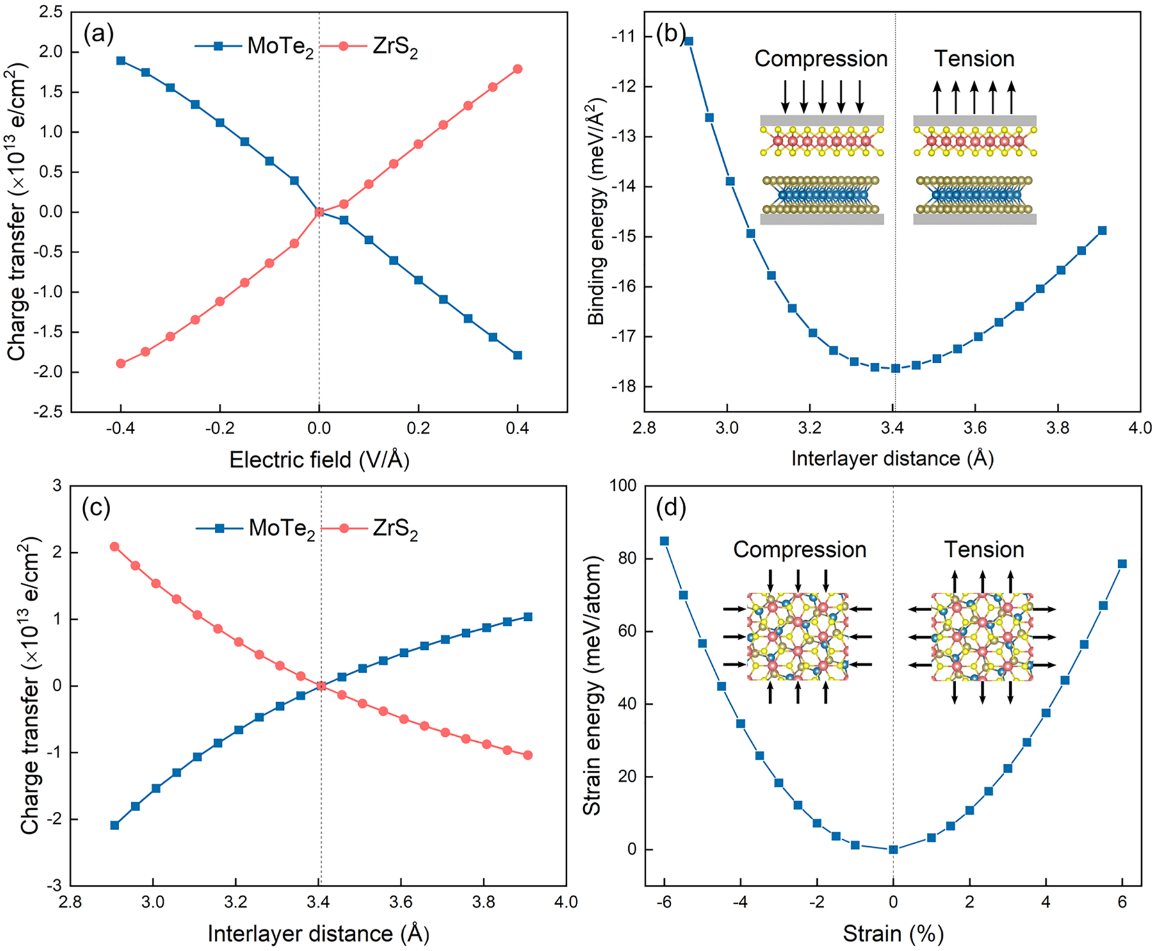

Figure 5. Charge transfers between $MoTe_2$ and ZrS_2 monolayers in the presence of E_{ext}. The charge of the monolayers in the heterobilayer in the absence of E_{ext} is used as a reference (a). Binding energies and charge transfers between $MoTe_2$ and ZrS_2 monolayers under out-of-plane strains. The charge of the monolayers in the strain-free heterobilayer is used as a reference (b, c). Strain energies of heterobilayers under in-plane biaxial strains (d). SOC is included in the calculations.

heterobilayers under various electric fields. For $E_{ext} > 0$, the band edge positions of $MoTe_2$ (ZrS_2) are pushed upward (downward) with respect to the Fermi level, and by increasing the positive electric fields, the band edge shifts are also increased. Using the PBE functional with SOC, changing the electric field strength from 0.1 to 0.4 V/Å, the energy difference between the ZrS_2 CB minimum and the $MoTe_2$ VB maximum changes from −0.06 to −0.12 eV. Smaller energy differences correspond to larger overlaps between the ZrS_2 low-lying conduction bands and the $MoTe_2$ high-lying valence bands. Consequently, more electrons can tunnel from the one layer to the other. Notably, the opposite behavior is found for electric fields pointed from ZrS_2 to $MoTe_2$, and for negative electric fields a transition from the type-III to the type-II band alignment is observed. Because the interlayer distance of the heterobilayer is ∼3.1 Å, the maximum electric field of 0.4 V/Å corresponds to a potential difference of about 1.2 V. Although this value may appear to be large, it is within the range of electric fields considered in experiments.[41] For calculations without SOC we find similar results (see the Supporting Information, Figure S20).

Similar calculations are also performed for the low-strained heterobilayer with rotated layers. In line with the previous results, positive electric fields lead to the larger overlap between the VB and CB states, whereas negative electric fields result in the opening of the band gap, as shown in Figure 4. For calculations without SOC we find similar results (see the Supporting Information, Figure S21). It is worth mentioning that for this model the interlayer distance is ∼3.4 Å and the maximum electric field of 0.4 V/Å corresponds to a potential difference of ∼1.4 V. Figure 5a shows the Bader charge transfer between the layers in the presence of electric fields of different strengths. For positive (negative) electric fields the electron transfer from $MoTe_2$ to ZrS_2 increases (decreases). These results are consistent with the band structure calculations, and the findings are verified by computing the corresponding charge density differences (see the Supporting Information, Figure S22).

3.3. Application of Out-of-Plane and In-Plane Strain.

Strain has been widely used for modifying materials properties, and low-dimensional materials can typically tolerate larger strains as compared to their bulk counterparts. For our analysis, low-strain $MoTe_2/ZrS_2$ heterobilayers with rotated layers are considered. As a first step we explore vertical strains, and taking as a reference the ground-state structure, d_{int} is either decreased or increased by up to 0.5 Å. Upon relaxation, Te atoms of the upper layer and S atoms of the lower layer can move along the *ab*-plane, and the rest of the atoms can freely move.

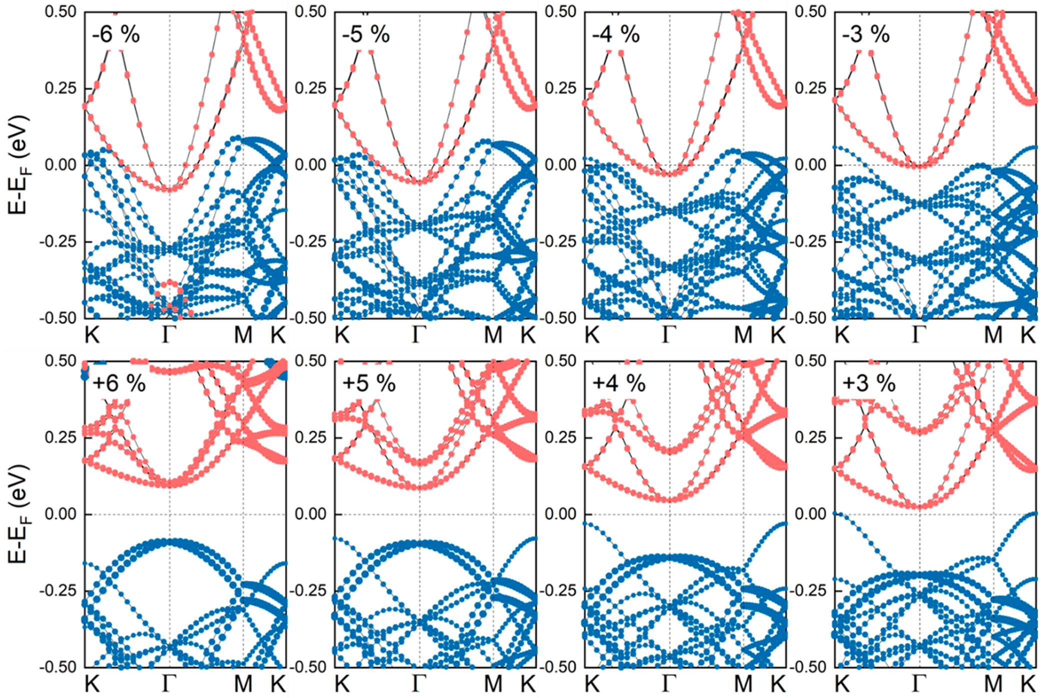

Figure 6. Electronic band structures of low-strained $MoTe_2/ZrS_2$ heterobilayers with rotated layers under in-plane strains. Positive strains refer to tension whereas negative strains refer to compression. Blue (orange) lines refer to contributions from $MoTe_2$ (ZrS_2) monolayers. SOC is included in the calculations.

Figure 5 shows the binding energies of the strained heterobilayers as well as the Bader charge transfers between the layers. The binding energies of the strained systems are found to be negative, which indicates their structural stability. For tensile strains the electron transfer from $MoTe_2$ to ZrS_2 decreases due to the decreased coupling between the layers, contrary to the results found for compressive strains. Notably, these observations are consistent with the charge density difference computations (see the Supporting Information, Figure S23). With regard to the electronic properties, no major variations are observed in the energies of the VB and CB edges with respect to the Fermi level for the low vertical stain considered in our study. For interlayer distances slightly lower than the equilibrium value of ∼3.4 Å, a small downward shift of the VB edge and a small upward shift of the CB are observed (see the Supporting Information, Figures S24 and S25).

Besides the out-of-plane strain, in-plane strained heterobilayers are also explored. The biaxial in-plane strain is defined by $\varepsilon = (a - a_0)/a_0 \times 100\%$, where a and a_0 correspond to the lattice parameters of the strained and pristine heterobilayers, respectively, whereas negative and positive values refer to compression and tension, respectively. Upon relaxation, all atoms are allowed to freely move whereas the lattice parameters remain unchanged.

The strain energies are calculated using the formula $E_S = E_{st} - E_{unst}$, where E_{st} and E_{unst} refer to the total energies of the heterobilayers with and without strain, respectively. As shown in Figure 5d, by increasing the tensile or compressive strains, an increase of the strain energy is observed. Furthermore, E_S variation resembles a quadratic curve, indicating an elastic deformation of the strained systems. For compressive strains, the high-lying VB states of $MoTe_2$ exhibit larger overlap with the low-lying CB states of ZrS_2, as compared to the strain-free heterobilayer, whereas the opposite behavior is found for tensile strains, as shown in Figure 6. For calculations without SOC we find similar results (see the Supporting Information, Figure S26).

Next, we briefly discuss the impact of strain on the electronic properties of (1×1) $MoTe_2$/(1×1) ZrS_2 heterobilayers. For the pristine heterobilayer $MoTe_2$ and ZrS_2 are already strained by about 2%, and a stack deformed by, e.g., 4% refers to $MoTe_2$ and ZrS_2 layers deformed by about 6 and 2%, respectively. First, the impact of strain (up to 6%) on the electronic properties of $MoTe_2$ and ZrS_2 isolated layers is investigated. With regard to ZrS_2, the band gap decreases upon compressive strain and increases upon tensile strain, and these results are in excellent agreement with previously reported theoretical calculations.[42] Concerning $MoTe_2$, tensile strain results in smaller band gaps, and the topmost valence band at Γ-point is shifted upward, which is in line with previously reported findings.[43] The band structures of the strained heterobilayers are approximate combinations of the band structures of the strained noninteracting monolayers, and the broken gap is preserved for the studied strained systems (see the Supporting Information, Figures S27 and S28).

4. CONCLUSIONS

In this paper, using first-principles calculations based on density functional theory, we explored the electronic properties of $MoTe_2/ZrS_2$ heterostructures with various stacking patterns and various thicknesses. Our simulations revealed that upon forming the heterostructure electrons spontaneously flow from $MoTe_2$ to ZrS_2, and the system resembles an ultrascaled parallel plate capacitor with an intrinsic electric field pointed from $MoTe_2$ to ZrS_2. We found that the VB and CB edges originated from $MoTe_2$ and ZrS_2 layers, respectively, were almost aligned, leading to the broken gap band alignment. The effects of strain and external electric fields on the electronic properties were also investigated. Notably, by increasing the positive electric fields, a larger overlap between the $MoTe_2$ valence bands and the ZrS_2 conduction bands was observed, leading to a larger band-to-band tunneling current. Low-strained heterostructures with various rotation angles between the constituent layers were also studied, and we found only small variations in the energies of the VB and CB edges with respect to the Fermi level for different rotation angles up to 30°.

■ ASSOCIATED CONTENT

Supporting Information

The Supporting Information is available free of charge at https://pubs.acs.org/doi/10.1021/acsami.2c13151.

> Atomic structures of (1×1) $MoTe_2/(1 \times 1)$ ZrS_2 heterobilayers and their band structures with and without SOC; interlayer distances and relative total energies of (1×1) $MoTe_2/(1 \times 1)$ ZrS_2 heterobilayers; band alignment of various 2D materials with respect to the vacuum level; atomic structures of low-strained heterobilayers with different rotation angles and their band structures with SOC; atomic structures of heterostacks composed of bilayer materials and their band structures with and without SOC; interlayer distances and relative total energies of heterostacks composed of bilayer materials; atomic structure of the R-stacked bilayer $MoTe_2$ and its band structure with SOC; atomic structures of heterostacks composed of monolayer and bilayer materials and their band structures with and without SOC; atomic structures of heterostacks composed of monolayer and trilayer/tetralayer materials and their band structures with and without SOC; band structures without SOC of (1×1) $MoTe_2/(1 \times 1)$ ZrS_2 heterobilayers and low-strained heterobilayers in the presence of external electric fields; charge density differences of low- strained heterobilayers under external electric fields and vertical strains; band structures of low-strained heterobilayers under out-of-plane strain with and without SOC; band structures of low-strained heterobilayers under in-plane strain without SOC; band structures of (1×1) $MoTe_2/(1 \times 1)$ ZrS_2 heterobilayers under in-plane strains and the corresponding band structures of the isolated stained monolayers with SOC (PDF)

■ AUTHOR INFORMATION

Corresponding Author

Konstantina Iordanidou – *Department of Physics, Chalmers University of Technology, SE-412 96 Gothenburg, Sweden;* orcid.org/0000-0003-4696-8204;
Email: konstantina.iordanidou@chalmers.se

Authors

Richa Mitra – *Department of Microtechnology and Nanoscience, Chalmers University of Technology, SE-412 96 Gothenburg, Sweden*
Naveen Shetty – *Department of Microtechnology and Nanoscience, Chalmers University of Technology, SE-412 96 Gothenburg, Sweden*
Samuel Lara-Avila – *Department of Microtechnology and Nanoscience, Chalmers University of Technology, SE-412 96 Gothenburg, Sweden;* orcid.org/0000-0002-8331-718X
Saroj Dash – *Department of Microtechnology and Nanoscience, Chalmers University of Technology, SE-412 96 Gothenburg, Sweden;* orcid.org/0000-0001-7931-4843
Sergey Kubatkin – *Department of Microtechnology and Nanoscience, Chalmers University of Technology, SE-412 96 Gothenburg, Sweden;* orcid.org/0000-0001-8551-9247
Julia Wiktor – *Department of Physics, Chalmers University of Technology, SE-412 96 Gothenburg, Sweden;* orcid.org/0000-0003-3395-1104

Complete contact information is available at:
https://pubs.acs.org/10.1021/acsami.2c13151

Notes

The authors declare no competing financial interest.

■ ACKNOWLEDGMENTS

We acknowledge funding from the 2DTech Vinnova Competence center at Chalmers University of Technology, the "Area of Advance – Energy", and the Gender Initiative for Excellence (Genie). For the computations we used resources provided by the Swedish National Infrastructure for Computing (SNIC) at NSC, C3SE, and PDC.

■ REFERENCES

(1) Bernstein, K.; Cavin, R. K.; Porod, W.; Seabaugh, A. C.; Welser, J. Device and Architectures Outlook for Beyond CMOS Switches. *Proc. IEEE* **2010**, *98*, 2169–2184.

(2) Seabaugh, A. C.; Zhang, Q. Low Voltage Tunnel Transistors for Beyond CMOS Logic. *Proc. IEEE* **2010**, *98*, 2095–2110.

(3) Ionescu, A. M.; Riel, H. Tunnel Field-Effect Transistors as Energy-Efficient Electronic Switches. *Nature* **2011**, *479*, 329.

(4) Diao, M.; Li, H.; Hou, R.; Liang, Y.; Wang, J.; Luo, Z.; Huang, Z.; Zhang, C. Vertical Heterostructure of SnS–MoS_2 Synthesized by Sulfur-Preloaded Chemical Vapor Deposition. *ACS Appl. Mater. Interfaces* **2020**, *12*, 7423–7431.

(5) Coy Diaz, H.; Avila, J.; Chen, C.; Addou, R.; Asensio, M. C.; Batzill, M. Direct Observation of Interlayer Hybridization and Dirac Relativistic Carriers in Graphene/MoS_2 van der Waals Heterostructures. *Nano Lett.* **2015**, *15*, 1135–1140.

(6) Muñoz, R.; López-Elvira, E.; Munuera, C.; Frisenda, R.; Sánchez-Sánchez, C.; Martín-Gago, J.Á.; García-Hernández, M. Direct Growth of Graphene-MoS_2 Heterostructure: Tailored Interface for Advanced Devices. *Appl. Surf. Sci.* **2022**, *581*, 151858.

(7) Aretouli, K. E.; Tsoutsou, D.; Tsipas, P.; Marquez-Velasco, J.; Aminalragia Giamini, S.; Kelaidis, N.; Psycharis, V.; Dimoulas, A. Epitaxial 2D $SnSe_2$/2D WSe_2 van der Waals Heterostructures. *ACS Appl. Mater. Interfaces* **2016**, *8*, 23222.

(8) Tsoutsou, D.; Aretouli, K. E.; Tsipas, P.; Marquez-Velasco, J.; Xenogiannopoulou, E.; Kelaidis, N.; Aminalragia Giamini, S.; Dimoulas, A. Epitaxial 2D $MoSe_2$ ($HfSe_2$) Semiconductor/2D $TaSe_2$ Metal van der Waals Heterostructures. *ACS Appl. Mater. Interfaces* **2016**, *8*, 1836.

(9) Duong, N. T.; Lee, J.; Bang, S.; Park, C.; Lim, S. C.; Jeong, M. S. Modulating the Functions of $MoS_2/MoTe_2$ van der Waals Heterostructure via Thickness Variation. *ACS Nano* **2019**, *13*, 4478–4485.

(10) Wang, J.; Jia, R.; Huang, Q.; Pan, C.; Zhu, J.; Wang, H.; Chen, C.; Zhang, Y.; Yang, Y.; Song, H.; Miao, F.; Huang, R. Vertical WS_2/SnS_2 van der Waals Heterostructure for Tunneling Transistors. *Sci. Rep.* **2018**, *8*, 1–9.

(11) Fiori, G.; Bonaccorso, F.; Iannaccone, G.; Palacios, T.; Neumaier, D.; Seabaugh, A.; Banerjee, S. K.; Colombo, L. Electronics Based on Two-Dimensional Materials. *Nat. Nanotechnol.* **2014**, *9*, 768–779.

(12) Thiele, S.; Kinberger, W.; Granzner, R.; Fiori, G.; Schwierz, F. The Prospects of Transition Metal Dichalcogenides for Ultimately Scaled CMOS. *Solid-State Electron.* **2018**, *143*, 2.

(13) Iannaccone, G.; Bonaccorso, F.; Colombo, L.; Fiori, G. Quantum Engineering of Transistors Based on 2D Materials Heterostructures. *Nat. Nanotechnol.* **2018**, *13*, 183.

(14) Afzalian, A.; Akhoundi, E.; Gaddemane, G.; Duflou, R.; Houssa, M. Advanced DFT−NEGF Transport Techniques for Novel 2-D Material and Device Exploration Including HfS_2/WSe_2 van der Waals Heterojunction TFET and WTe_2/WS_2 Metal/Semiconductor Contact. *IEEE Trans. Electron Devices* **2021**, *68*, 5372.

(15) Zeng, Z.; Yin, Z.; Huang, X.; Li, H.; He, Q.; Lu, G.; Boey, F.; Zhang, H. Single-Layer Semiconducting Nanosheets: High-Yield Preparation and Device Fabrication. *Angew. Chem.* **2011**, *123*, 11289−11293.

(16) Coleman, J. N.; Lotya, M.; O'Neill, A.; Bergin, S. D.; King, P. J.; Khan, U.; Young, K.; Gaucher, A.; De, S.; Smith, R. J.; Shvets, I. V.; et al. Two-Dimensional Nanosheets Produced by Liquid Exfoliation of Layered. *Mater. Sci.* **2011**, *331*, 568−571.

(17) Zhang, W.; Huang, Z.; Zhang, W.; Li, Y. Two-Dimensional Semiconductors with Possible High Room Temperature Mobility. *Nano Res.* **2014**, *7*, 1731−1737.

(18) Iordanidou, K.; Wiktor, J. Two-Dimensional $MoTe_2$/$SnSe_2$ van der Waals Heterostructures for Tunnel-FET Applications. *Phys. Rev. Mater.* **2022**, *6*, 084001.

(19) Kresse, G.; Furthmüller, J. Efficient Iterative Schemes for Ab Initio Total-Energy Calculations Using a Plane-Wave Basis Set. *Phys. Rev. B* **1996**, *54*, 11169.

(20) Kresse, G.; Furthmüller, J. Efficiency of Ab-Initio Total Energy Calculations for Metals and Semiconductors Using a Plane-Wave Basis Set. *Comput. Mater. Sci.* **1996**, *6*, 15−50.

(21) Blöchl, P. E. Projector Augmented-Wave Method. *Phys. Rev. B* **1994**, *50*, 17953.

(22) Lazić, P. CellMatch: Combining Two-Unit Cells into a Common Supercell with Minimal Strain. *Comput. Phys. Commun.* **2015**, *197*, 324−334.

(23) Hamada, I. van der Waals Density Functional Made Accurate. *Phys. Rev. B* **2014**, *89*, 121103.

(24) Perdew, J. P.; Burke, K.; Ernzerhof, M. Generalized Gradient Approximation Made Simple. *Phys. Rev. Lett.* **1996**, *77*, 3865.

(25) Li, W. F.; Fang, C.; van Huis, M. A. Strong Spin-Orbit Splitting and Magnetism of Point Defect States in Monolayer WS_2. *Phys. Rev. B* **2016**, *94*, 195425.

(26) Heyd, J.; Scuseria, G. E.; Ernzerhof, M. Hybrid Functionals Based on a Screened Coulomb. *Potential. J. Chem. Phys.* **2003**, *118*, 8207−8215.

(27) Klimeš, J.; Bowler, D. R.; Michaelides, A. Van der Waals Density Functionals Applied to Solids. *Phys. Rev. B* **2011**, *83*, 195131.

(28) Berland, K.; Hyldgaard, P. Exchange Functional that Tests the Robustness of the Plasmon Description of the van der Waals Density Functional. *Phys. Rev. B* **2014**, *89*, 035412.

(29) Grimme, S.; Antony, J.; Ehrlich, S.; Krieg, H. A Consistent and Accurate Ab Initio Parametrization of Density Functional Dispersion Correction (DFT-D) for the 94 Elements H-Pu. *J. Chem. Phys.* **2010**, *132*, 154104.

(30) Lu, A. K. A.; Houssa, M.; Radu, I. P.; Pourtois, G. Toward an Understanding of the Electric Field-Induced Electrostatic Doping in van der Waals Heterostructures: A First-Principles Study. *ACS Appl. Mater. Interfaces* **2017**, *9*, 7725−7734.

(31) Mao, X.; Li, J.; Liu, Z.; Wang, G.; Zhang, Q.; Jin, Y. T-Phase and H-Phase Coupled TMD van der Waals Heterostructure ZrS_2/$MoTe_2$ with Both Rashba Spin Splitting and Type-III Band Alignment. *J. Phys. Chem. C* **2022**, *126*, 10601.

(32) Zhang, C.; Gong, C.; Nie, Y.; Min, K.-A.; Liang, C.; Oh, Y. J.; Zhang, H.; Wang, W.; Hong, S.; Colombo, L.; Wallace, R. M; Cho, K. Systematic Study of Electronic Structure and Band Alignment of Monolayer Transition Metal Dichalcogenides in van der Waals Heterostructures. *2D Mater.* **2017**, *4*, 015026.

(33) Reddy, B. A.; Ponomarev, E.; Gutiérrez-Lezama, I.; Ubrig, N.; Barreteau, C.; Giannini, E.; Morpurgo, A. F. Synthetic Semimetals with van der Waals Interfaces. *Nano Lett.* **2020**, *20*, 1322.

(34) Iordanidou, K.; Persson, C. Optoelectronic properties of coexisting InGaZnO4 structures. *Mater. Sci. Semicond. Process* **2021**, *121*, 105297.

(35) Zhang, L.; Zhang, Z.; Wu, F.; Wang, D.; Gogna, R.; Hou, S.; Watanabe, K.; Taniguchi, T.; Kulkarni, K.; Kuo, T.; Forrest, S. R.; Deng, H. Twist-Angle Dependence of Moiré Excitons in WS_2/$MoSe_2$ Heterobilayers. *Nat. Commun.* **2020**, *11*, 1−8.

(36) Cai, X.; An, L.; Feng, X.; Wang, S.; Zhou, Z.; Chen, Y.; Cai, Y.; Cheng, C.; Pan, X.; Wang, N. Layer-Dependent Interface Reconstruction and Strain Modulation in Twisted WSe_2. *Nanoscale* **2021**, *13*, 13624−13630.

(37) Wu, F.; Lovorn, T.; Tutuc, E.; Martin, I.; MacDonald, A. H. Topological Insulators in Twisted Transition Metal Dichalcogenide Homobilayers. *Phys. Rev. Lett.* **2019**, *122*, 086402.

(38) He, J.; Hummer, K.; Franchini, C. Stacking effects on the Electronic and Optical Properties of Bilayer Transition Metal Dichalcogenides MoS_2, $MoSe_2$, WS_2, and WSe_2. *Phys. Rev. B* **2014**, *89*, 075409.

(39) Lin, Z.; Si, C.; Duan, S.; Wang, C.; Duan, W. Rashba Splitting in Bilayer Transition Metal Dichalcogenides Controlled by Electronic Ferroelectricity. *Phys. Rev. B* **2019**, *100*, 155408.

(40) Shang, J.; Huang, L.; Wei, Z. Effects of Vertical Electric Field and Compressive Strain on Electronic Properties of Bilayer ZrS_2. *J. Semicond.* **2017**, *38*, 033001.

(41) Chu, T.; Ilatikhameneh, H.; Klimeck, G.; Rahman, R.; Chen, Z. Electrically Tunable Bandgaps in Bilayer MoS_2. *Nano Lett.* **2015**, *15*, 8000−8007.

(42) Lv, H. Y.; Lu, W. J.; Shao, D. F.; Lu, H. Y.; Sun, Y. P. Strain-Induced Enhancement in the Thermoelectric Performance of a ZrS_2 Monolayer. *J. Mater. Chem. C* **2016**, *4*, 4538−4545.

(43) Postorino, S.; Grassano, D.; D'Alessandro, M.; Pianetti, A.; Pulci, O.; Palummo, M. Strain-Induced Effects on the Electronic Properties of 2D Materials. *Nanomater. Nanotechnol.* **2020**, *10*, 184798042090256.

(44) Wang, V.; Xu, N.; Liu, J. C.; Tang, G.; Geng, W. T. VASPKIT: A User-Friendly Interface Facilitating High-Throughput Computing and Analysis Using VASP Code. *Comput. Phys. Commun.* **2021**, *267*, 108033.

https://doi.org/10.1021/acsami.2c13151